

Recent human-induced atmospheric drying across Europe unprecedented in the last 400 years

Received: 3 February 2023

Accepted: 24 October 2023

Published online: 27 December 2023

 Check for updates

A list of authors and their affiliations appears at the end of the paper

The vapor pressure deficit reflects the difference between how much moisture the atmosphere could and actually does hold, a factor that fundamentally affects evapotranspiration, ecosystem functioning, and vegetation carbon uptake. Its spatial variability and long-term trends under natural *versus* human-influenced climate are poorly known despite being essential for predicting future effects on natural ecosystems and human societies such as crop yield, wildfires, and health. Here we combine regionally distinct reconstructions of pre-industrial summer vapor pressure deficit variability from Europe's largest oxygen-isotope network of tree-ring cellulose with observational records and Earth system model simulations with and without human forcing included. We demonstrate that an intensification of atmospheric drying during the recent decades across different European target regions is unprecedented in a pre-industrial context and that it is attributed to human influence with more than 98% probability. The magnitude of this trend is largest in Western and Central Europe, the Alps and Pyrenees region, and the smallest in southern Fennoscandia. In view of the extreme drought and compound events of the recent years, further atmospheric drying poses an enhanced risk to vegetation, specifically in the densely populated areas of the European temperate lowlands.

Vapor pressure deficit, VPD, represents the difference between the amount of moisture that the air can hold at saturation (saturation vapor pressure, e_s) and its actual moisture content (actual vapor pressure, e_a)¹. In a warming atmosphere e_s increases, whereas changes in e_a are less uniform: The vapor content of the atmosphere is driven by complex ocean-land-atmosphere water exchange mechanisms and recycling processes, that is, the rate at which vapor is supplied to the atmosphere via both ocean evaporation and land surface evapotranspiration, and the strength of this ocean-land-atmosphere coupling². High VPD can cause increased rates of water loss from soils and subsequent heating of the terrestrial surfaces via soil moisture-temperature feedback mechanisms^{3,4}. VPD as a climate variable is therefore of fundamental ecological

and socio-economic importance due to its effects on evapotranspiration and surface heat fluxes and, coupled with heatwaves, amplification of drought events with severe consequences on for example, vegetation functioning⁵, crop yield⁶ and subsequently human health⁷.

A general increase in VPD over the past decades has already been reported at a global scale⁸, accelerating soil drought^{9,10}, plant water stress¹¹, vegetation mortality^{12,13} and forest fires¹⁴. Its spatial evolution, long-term natural background variability and potential attribution to human influence are, however, still unclear. Hence, uncertainties in predictions of future VPD variability and its effects on the coupled carbon-water cycle and surface climate feedbacks by Earth system models (ESMs) are also high.

✉ e-mail: kerstin.treydte@wsl.ch.

Here we combine empirical proxy data covering 400 years of pre-industrial and recent summer VPD variability with meteorological observations and ESM simulations to investigate spatio-temporal VPD patterns across Europe and understand their natural *versus* human-induced variability. This knowledge will contribute to reducing uncertainties in simulating future climate scenarios and help estimating the potential threat of high VPD levels to ecosystems, economies, and societies.

Empirical proxy data are represented by a European network of oxygen isotope ratios ($\delta^{18}\text{O}$) in tree-ring cellulose from 45 sites spanning a latitudinal gradient from northern Fennoscandia to the Mediterranean (Fig. 1). This network is unprecedented in terms of spatial coverage, number of sites, and composition of annually resolved multi-century long $\delta^{18}\text{O}$ chronologies. Sites range from temperate lowland over boreal and alpine to Mediterranean climates and contain seven tree genera, with oaks and pines most represented (Fig. 1, Extended Data Table 1). While coniferous sites are distributed across the whole network, broadleaf sites concentrate in the mid latitudes of western and eastern central Europe.

We explicitly utilize pure tree-ring $\delta^{18}\text{O}$ records instead of combining them with $\delta^{13}\text{C}$ records which was previously done for hydroclimatic reconstruction¹⁵. While combining both may be appealing due to their potentially strong inter-correlation in the high-frequency domain¹⁶, long-term trends in $\delta^{13}\text{C}$ records can be biased by non-climatic effects in the industrial period (20th/21st century) due to a response of stomatal conductance to the increase in atmospheric CO_2 concentration^{17,18}. Further, tree-ring $\delta^{13}\text{C}$ records are sensitive to tree size and stand dynamics, while $\delta^{18}\text{O}$ records are less sensitive to these factors¹⁹. Therefore, non-climatic trends are minimal to absent in pure tree-ring $\delta^{18}\text{O}$ records^{20–22}, and long-term climatic variation is preserved with high certainty.

Tree-ring $\delta^{18}\text{O}$ records have proven to be a particular robust climate proxy in temperate environments where traditional tree-ring parameters such as tree-ring width or maximum latewood density often underperform in recording hydroclimatic information²². They reflect the $\delta^{18}\text{O}$ variations of precipitation and soil water taken up by the roots, modified by a combination of climatic and physiological processes^{23–25}. Along these processes, evaporative enrichment of the heavy ^{18}O isotope along the atmosphere-soil-tree continuum is a key effect in generating a VPD-sensitive tree-ring $\delta^{18}\text{O}$ signature²⁶. While the potential of tree-ring $\delta^{18}\text{O}$ to record VPD variations has been demonstrated^{27–31}, no robust reconstruction attempt has been made with the aim of placing recent VPD variability in a pre-industrial context.

Our spatially and temporally robust reconstructions of summer VPD variability for different independent European target regions combined with meteorological records and ESM simulations allow exploring the following questions: 1) Is the VPD increase observed across large parts of Europe in recent decades unprecedented in the pre-industrial context, and if so, 2) is it likely attributable to human-induced climate change? For that we compared the range and variability of i) reconstructed VPD values for the preindustrial period and ESM simulations without human induced forcing with ii) recent observations of VPD and ESM results including human forcing and implementing systematic attribution assessment³².

Network response to climate

The distribution of mean $\delta^{18}\text{O}$ values across the network represents the geographic location of the sites along latitudinal, longitudinal, and altitudinal gradients, with the effect of geographical location exceeding any effect of species (Extended Data Fig. 1). Climate signals recorded in the individual site chronologies are consistent across the geographical range of the network, with highest correlations observed with VPD. Summer climate conditions (June to August, JJA) during the year of ring formation are the key driver of tree-ring $\delta^{18}\text{O}$ variability for both deciduous species and conifers, and climatic conditions of the previous year are of minor relevance (Extended Data Fig. 2). The strength of the

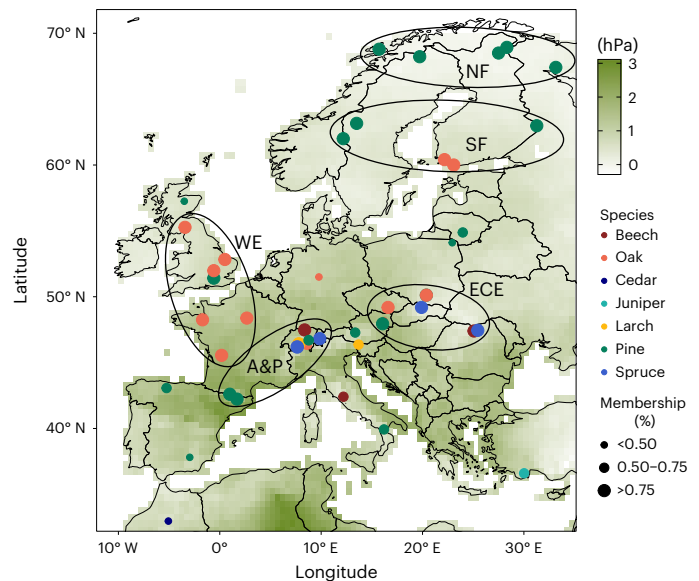


Fig. 1 Distribution of 45 tree-ring cellulose $\delta^{18}\text{O}$ chronologies across Europe, spatial clustering and changes in observed European summer VPD. Dot sizes indicate the contribution (membership in %) of the individual site chronologies to the common variance of a given cluster based on fuzzy cluster analysis (Extended Data Fig. 5). The chronologies are separated into five independent target regions, that is, northern Fennoscandia (NF), southern Fennoscandia (SF), western Europe (WE), eastern central Europe (ECE) and Alps & Pyrenees (AP). Green shadings represent differences in mean observational VPD between the period 1920-1990 and 1991-2020 calculated for each grid point based on the CRU TS 4.05 dataset. Map source: R package ggplot2 (<https://ggplot2.tidyverse.org>), R-version 4.1.2.

relationship is neither affected by the geographic location (Extended Data Fig. 3) nor the general climatic conditions represented by the long-term means of various climate variables (Extended Data Fig. 4), except at the southern and north-western edge of the network. Summer VPD was selected as the target variable for climate reconstruction due to its i) strongest spatial and temporal robustness (Fig. 2a, Extended Data Fig. 2, Supplementary Table 2), and ii) its climatic and eco-physiological importance.

Spatio-temporal robustness of the VPD signal across Europe

Fuzzy cluster analysis revealed grouping of the site $\delta^{18}\text{O}$ chronologies in five distinctly different geographic regions (Fig. 1, Extended Data Fig. 5): northern Fennoscandia (NF), southern Fennoscandia (SF), western Europe (WE), eastern central Europe (ECE), and the Alps & Pyrenees (AP). For subsequent nested principal component (PC) analysis, only chronologies that contributed >75% to the corresponding cluster were retained to ensure independence between the regional reconstructions. The common variance explained by PC1 (common period 1920-1994) varied between 61% for WE, 64% for ECE, 61% for AP, 62% for SF, and 45% for NF.

Spatial correlation fields calculated between nested PC1 of each regional cluster and gridded summer VPD data confirmed the spatial coherence of the VPD signal in tree-ring $\delta^{18}\text{O}$ on a continental scale (Fig. 2). All five geographic regions corresponded spatially to the areas with the highest correlations (Fig. 2b–f). For NF, however, the strength and spatial extent of the correlation with summer VPD was less pronounced compared to the other regions. Dipole-like correlation patterns emerged between eastern central Europe and Fennoscandia (Fig. 2d, e) and between southwestern and eastern Europe (Fig. 2c).

The strength and temporal robustness of the summer VPD signal in our tree-ring $\delta^{18}\text{O}$ proxies further increased when calculated for

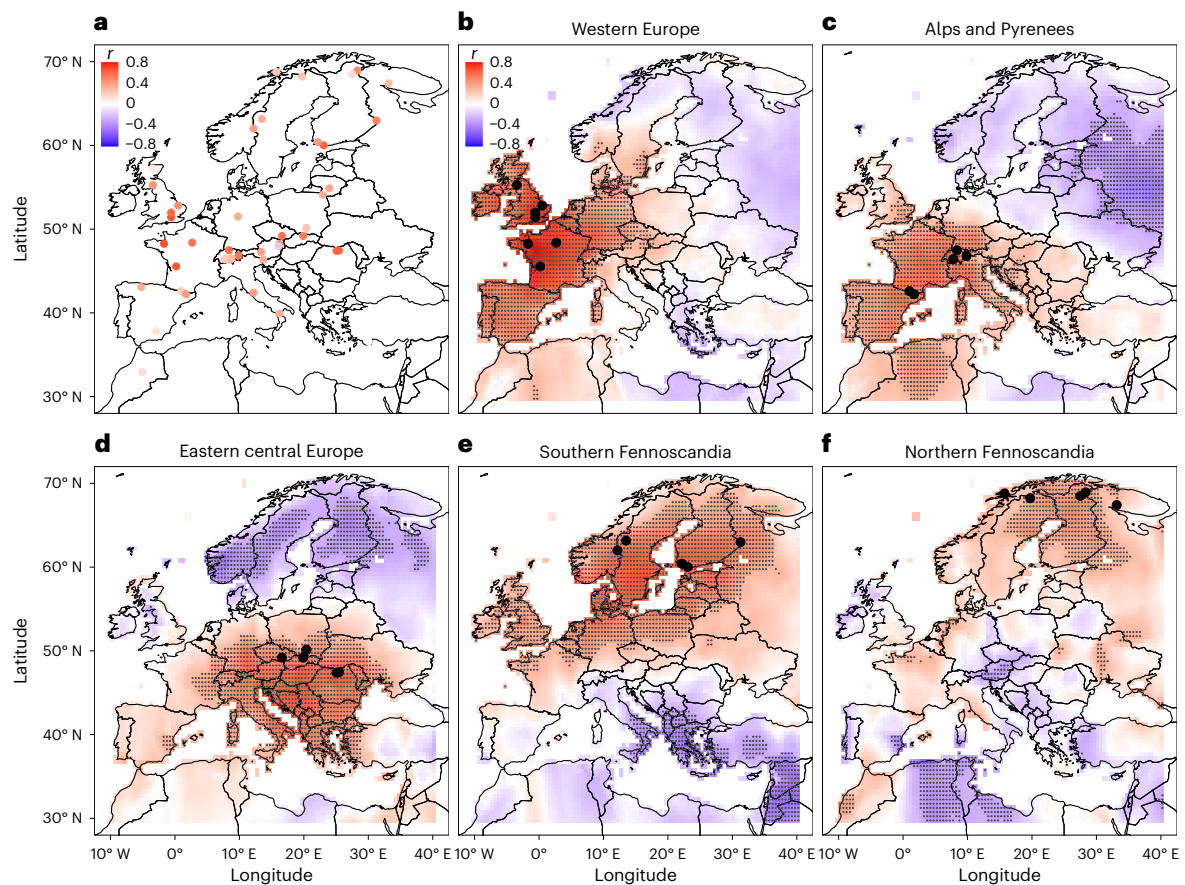


Fig. 2 | Spatial extend of the summer VPD signal in five European target regions. **a**) Correlation between individual site $\delta^{18}\text{O}$ chronologies and the closest summer VPD gridpoint. **b–f**) Spatial correlation fields calculated between the PCI nests representing each of the five geographical regions derived from cluster analysis and gridded summer VPD (June–August). Large black dots indicate sites

contributing to the corresponding PCI nests of each regional cluster due to a membership exponent $>75\%$, small black dots display grid points with significant correlations at $P < 0.001$. Map source: R package ggplot2 (<https://ggplot2.tidyverse.org>), R-version 4.1.2.

the regional PCI records. Particularly the WE record displayed exceptionally high correlations ($P < 0.01$) for the full calibration period 1920–2000 ($r_{\text{full}} = 0.79$), as well as for the early (1920–1960) and late (1961–2000) periods separately ($r_{\text{early}} = 0.78$ and $r_{\text{late}} = 0.82$). The ECE record also showed highly significant ($P < 0.01$) and temporally stable correlations ($r_{\text{full}} = 0.65$; $r_{\text{early}} = 0.67$, $r_{\text{late}} = 0.63$), followed by the SF record ($r_{\text{full}} = 0.64$), with an increase of the correlations from the early to the late period ($r_{\text{early}} = 0.52$, $r_{\text{late}} = 0.72$) ($P < 0.01$). Also, for the AP record, correlations were highly significant ($P < 0.01$) ($r_{\text{full}} = 0.61$) and robust over time ($r_{\text{early}} = 0.65$, $r_{\text{late}} = 0.60$). The NF record showed lowest, though still highly significant correlations, but with differences between the full *versus* split period values ($r_{\text{full}} = 0.42$; $P < 0.05$; $r_{\text{early}} = 0.59$, $r_{\text{late}} = 0.52$; $P < 0.01$).

The temporal robustness of the summer VPD signal as evaluated by calibration-verification statistics allowed the development of regional PCI reconstructions (Fig. 3). This was done by scaling the spliced regional PCI nests to their VPD target over the full 1920–2000 calibration period. Particularly the WE record yielded excellent reconstruction skills (Supplementary Table 2, Supplementary Fig. 1) and the signal was also robust in ECE, SF and AP. While for NF R^2 -values were also still significant, other calibration-verification statistics failed, indicating inconsistencies in the long-term trends (Supplementary Table 2, Supplementary Fig. 1). This prevented the creation of a robust reconstruction for NF. While our reconstructions end in the 2000s, the strong calibration-verification statistics and scaling of the proxy to the variance and mean of the observations justified a direct combination with observational VPD in the period 1991–2020.

400 years of European summer VPD and human attribution

Historical periods of reconstructed high and low summer VPD expectedly varied between the four regions and only few common patterns appeared (Fig. 3): A transition from high to low VPD in the early 1600s until the 1640s occurred in all target regions; relatively low VPD occurred during the 1670s to 1720s in all regions except SF, and from the 1730s to 1750 in WE and ECE, with comparably high VPD in SF and AP. Another short dry period occurred at the end of the 19th century in all regions though less distinct in AP. In the early 20th century, a period with relatively high VPD appeared in all four regions in the late 1940s/early 1950s, albeit less distinct in SF, followed by low VPD in the 1970s/early 1980s except SF. The most outstanding single extreme in 400 years was 1709 (Fig. 3) as the year with lowest VPD in SF and WE, and also distinctly low values in ECE. Comparisons between observational as well as reconstructed summer VPD and North Atlantic Oscillation (NAO) indices revealed significant relationships ($P < 0.01$) in all four investigated regions (Supplementary Table 3).

During the recent decades of the 21st century VPD increased to unusually high levels in three of four reconstructions and the synchronicity of this increase was unprecedented in the 400-year context (Fig. 3). It has continued until 2020 to a level not reached in the previous 400 years across WE, ECE and most strongly AP, whereas less pronounced in SF. Within this recent period, highest VPD levels have been reached during the drought years of 2003, 2015 and 2018, that affected all four regions.

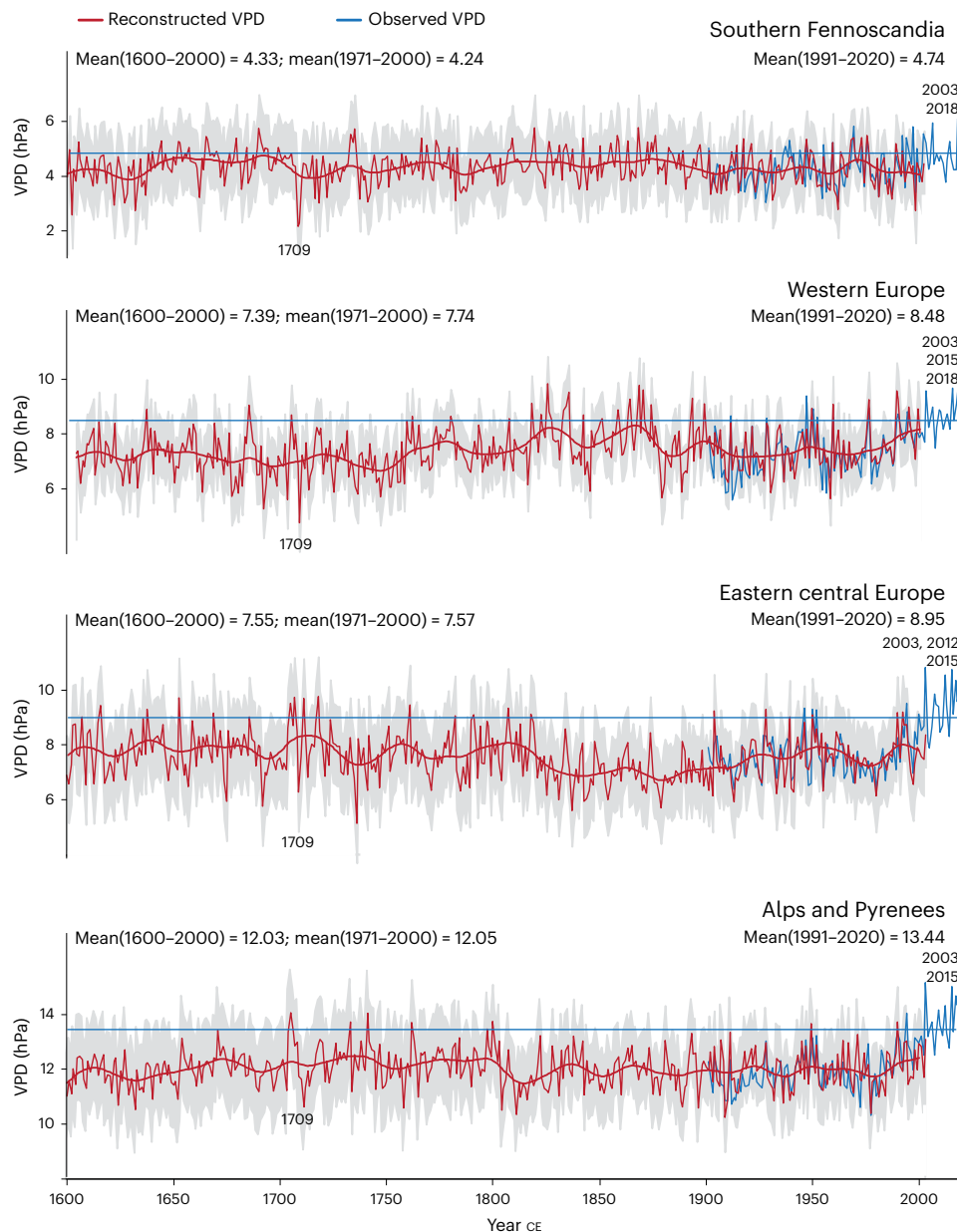


Fig. 3 | Reconstructed and observed summer (June–August) VPD for four European target regions. Horizontal blue lines indicate the mean of observed VPD for the period 1991–2020. Smoothed curves are 30-year splines with a frequency cut-off at 50%. Means and standard deviations (SD) are

given in hPa. Grey areas indicate the root mean square error spliced together from the individual PC1 nests per region. Details on the robustness of the $\delta^{18}\text{O}$ -VPD relationships in the calibration/verification period are provided in Supplementary Table 2 and Supplementary Fig. 1.

Comparison of our reconstructions plus observations with summer VPD simulations from twelve available Earth system models³³ (ESM) enabled independent confirmation of the unprecedented VPD increase of the recent 30-year period (1991–2020) and its attribution to human influence. Three main simulation types were considered: i) simulations forced with pre-industrial conditions, ii) simulations including both natural and anthropogenic historical forcing until 2014, and iii) simulations including a scenario of medium future greenhouse gas forcings.

Reconstructions and simulations agreed well in their distribution of normalized 30-year mean VPD values of the pre-industrial period (Fig. 4). Moreover, the multi-model means indicated with more than 98% probability in all regions that VPD levels of the current 30-year period (1991–2020) could only be reached when attributing them to human influence. Multi-model means simulated with historical natural forcing

excluding human influence were still well within the estimated ranges of pre-industrial variability (Supplementary Table 4). Although some individual ESMs simulated recent VPD values as high as the observations and others even lower than the pre-industrial average (Fig. 4; Supplementary Table 5), results from multi-model means were consistent. Observed normalized summer VPD means of the recent 1991–2020 period strongly exceeded pre-industrial values and were substantially higher than the multi-model means in all four regions (Extended Data Table 2). In comparison recent non-normalized VPD levels from the multi-model means generally agreed well with the observational levels (Supplementary Fig. 3). Sensitivity tests confirmed the robustness of our findings i) when analysing 10-year instead of 30-year means (Supplementary Fig. 4), ii) when estimating the baseline climate variability of pre-industrial VPD from consecutive non-overlapping periods in the simulations, instead of randomly sampled years (Supplementary Fig. 5),

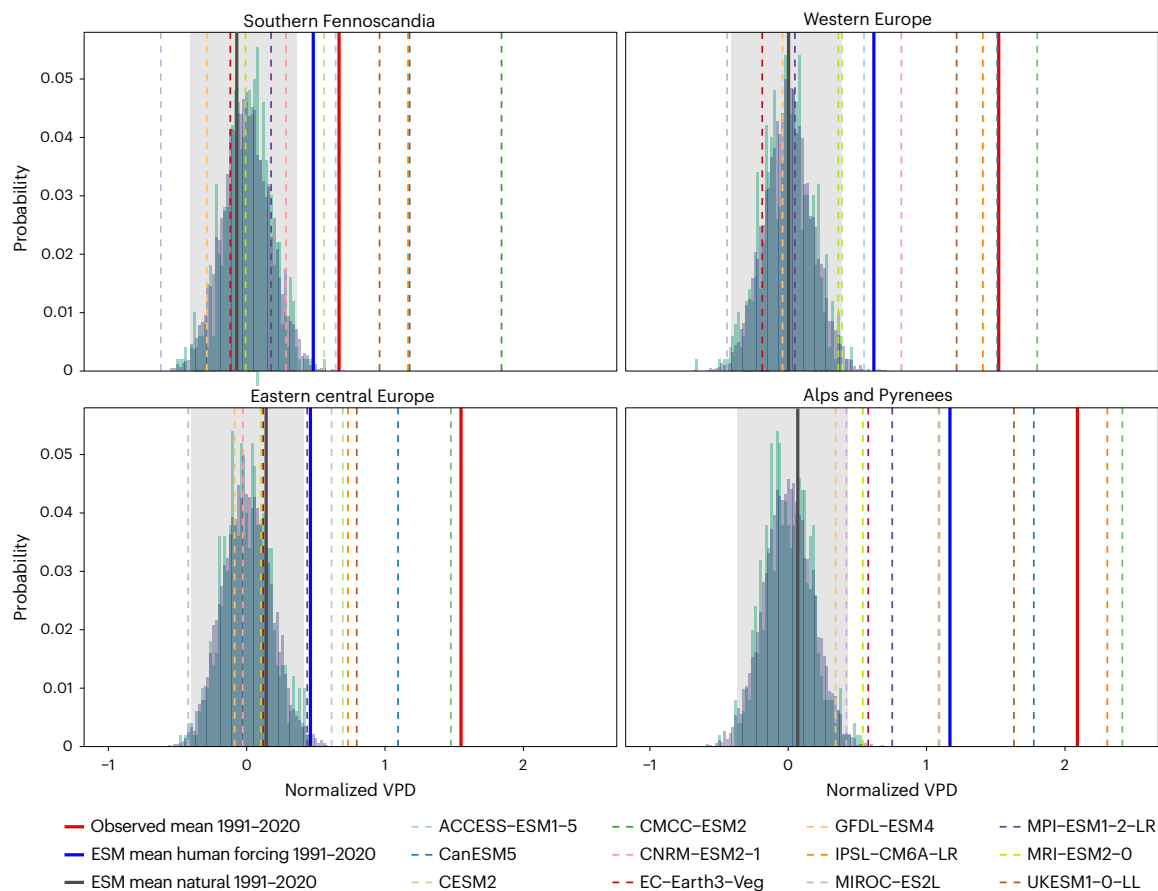


Fig. 4 | Unprecedented summer VPD increase in the context of pre-industrial natural variability and its attribution to human influence. Bars indicate pre-industrial natural variability from tree-ring $\delta^{18}\text{O}$ -based VPD reconstructions for the period 1600-1850 (green), and from 500-year simulations of 12 ESMs with no human-induced forcing included, piControl (blue). Grey shadows represent the 98% distribution range of natural variability. Solid lines indicate VPD during the most recent period 1991-2020 CE based on i) direct VPD observations (red), ii)

multi-model means of combined historical and ssp245 scenarios with human-induced forcing included (blue), and iii) multi-model means of the historical scenario with human-induced forcing excluded (green). Dashed lines are the individual model means for 1991-2020 based on combined historical and ssp245 scenarios with human-induced forcing included. VPD values are normalized for comparability. Source of model outputs: <https://esgf-node.llnl.gov/search/cmip6/>.

and iii) when using model simulations that exclude the influence of past land use/land cover (LULC) on recent VPD (Supplementary Table 6).

Recent summer VPD increase is unprecedented and human-induced

Summer drying of the atmosphere intensified in the recent decades and significantly exceeded pre-industrial conditions of the past 400 years across all European target regions, as indicated by a combination of tree-ring $\delta^{18}\text{O}$ -based reconstructions, gridded meteorological observations, and ESM simulations. The magnitude of the recent increase and the absolute VPD levels reached vary, however, among the four regions. Strongest atmospheric drying trends are seen in the southern, continental mountain regions of the Alps & Pyrenees, followed by the temperate lowlands of western and eastern Central Europe, whereas in southern Fennoscandia, this trend is less pronounced. Model simulations further demonstrate that the observed summer VPD level of the last 30 years would have been extremely unlikely to occur without ongoing human-induced climate change.

Potential atmospheric drivers of summer VPD patterns

Some synchronized periods of historical low and high VPD across Europe in our reconstructions, together with dipole-like spatial correlation fields and significant relationships to NAO indices indicate

a link between VPD and large-scale climate dynamics. The latitudinal position of the North Atlantic Jet during summer and the corresponding occurrence and duration of near-stationary atmospheric pressure fields ('atmospheric blocking') have been reported as major drivers of historical and recent dry and moist weather regimes over the North Atlantic-European domain³⁴⁻³⁶ and even as drivers of European forest productivity³⁴. Also, the increasing number of mid-latitude weather extremes in the recent decades have been associated with an enhanced latitudinal variability of the North Atlantic Jet³⁵. Such large-scale atmospheric modes could also serve as an explanation for the year 1709 with extremely low reconstructed VPD values. An exceptionally strong negative NAO phase has been reported for this year³⁶, with the most severe frost conditions of the past 500 years continuing even into early summer and extending widely across the European continent^{36,37}. Late soil thawing and ^{18}O -depleted 'cold' precipitation together with low atmospheric demand far into the growing season have allowed propagating this extreme event specifically into tree-ring $\delta^{18}\text{O}$ (but not into European-scale growth-based and combined $\delta^{13}\text{C}$ - $\delta^{18}\text{O}$ chronologies respectively, Supplementary Fig. 2).

Regional differences in the magnitude of the most recent VPD increase are interpreted here towards the nonstationary evolution of the actual vapor pressure in the air and an intensification of the water cycle under recent warming due to land-ocean-atmosphere feedback processes^{2,3,38}. In Fennoscandia, an increase in atmospheric moisture

has been reported over the past 30 years and can be specifically linked to changes in the dynamic processes of moisture supply from the oceanic source regions, such as increasing ocean evaporation³⁸ explaining the moderate increase in VPD observed there. In western and eastern central Europe and even more towards southern and continental regions such as the Alps & Pyrenees, a recent decrease in relative air humidity has been reported that is to a certain degree related to stronger differences between faster increasing air temperatures over land masses and slower increasing sea surface temperatures in the oceanic moisture region^{2,38}. Therefore, humidity of the air advected from oceans to land surfaces would not increase enough to maintain a constant e_a in these continental regions³⁹. The combination of increasing temperatures and constant or even decreasing e_a intensifies atmospheric drying beyond the effect of warming alone.

Ecological and socio-economic implications

Our reported VPD increase to the unprecedented levels of the recent years has major implications for land-atmosphere interactions, vegetation dynamics and carbon budgets, depending on the climatic region. In continental and Mediterranean areas VPD-driven declines in stomatal conductance lead to decreased evapotranspiration and thus to a further enhancement of air drying⁴ and can already represent a significant constraint on plant carbon uptake⁴⁰. Considering that forest canopy leaves are typically warmer than air and have limited ability to regulate temperature⁴¹, a leaf specific VPD increase may even exceed the increase in atmospheric VPD, with amplification of reduced carbon assimilation capacity and eventually heat damage. In other regions such as western and eastern central Europe an increase of tree-ring $\delta^{18}\text{O}$ sensitivity to summer VPD over the recent decades indicates continued high stomatal conductance and an amplification of evapotranspiration^{42–44} in correspondence with a large-scale intensification of the atmospheric moisture demand^{43,45}, and consequently, the hydrological cycle².

Recent studies already report a response shift of vegetation growth towards increased VPD sensitivity in the last few decades^{46–48}, including reductions in gross primary productivity⁴⁹, increased tree mortality^{13,50}, forest decline and yield reductions⁶. A further VPD increase will cause enhanced wildfire risk, modify wildfire regimes, and may transform regions that are currently fire-free into fire prone ecosystems³ such as the Pyrenees⁵¹ as one of our study regions.

Our findings may be viewed within the context of the recent wildfires and extreme drought-related events across many parts of Europe. If the atmosphere continues to dry, impacts on natural ecosystem services, the forestry and agricultural sector and human health are anticipated. Increased evaporation and associated changes in the amount and distribution of precipitation will disrupt water management infrastructure, affecting the availability, distribution, and quality of water, as well as the reliability of the resource for hydropower generation, irrigation, and human use. The direct and indirect effects of a drying atmosphere are likely to be far reaching and will require attention to minimize their future negative impacts.

Online content

Any methods, additional references, Nature Portfolio reporting summaries, source data, extended data, supplementary information, acknowledgements, peer review information; details of author contributions and competing interests; and statements of data and code availability are available at <https://doi.org/10.1038/s41561-023-01335-8>.

References

- Bohren, C. F., Albrecht, B. A. & Schroeder, D. V. Atmospheric thermodynamics. *Am. J. Phys.* **68**, 1159–1160 (2000).
- Douville, H et al. in *Climate Change 2021: The Physical Science Basis* (eds Masson-Delmotte, V. et al.) 1055–1210 (Cambridge Univ. Press, 2021).
- Seneviratne, S. I. et al. in *Climate Change 2021: The Physical Science Basis* (eds Masson-Delmotte, V. et al.) 1513–1766 (Cambridge Univ. Press, 2021).
- Seneviratne, S. I. et al. Investigating soil moisture-climate interactions in a changing climate: a review. *Earth Sci. Rev.* **99**, 125–161 (2010).
- Grossiord, C. et al. Plant responses to rising vapor pressure deficit. *N. Phytol.* **226**, 1550–1566 (2020).
- Hsiao, J. et al. Maize yield under a changing climate: the hidden role of vapor pressure deficit. *Agric. Meteorol.* **279**, 107692 (2019).
- Ranasinghe, R. et al. in *Climate Change 2021: The Physical Science Basis* (eds Masson-Delmotte, V. et al.) 1767–1926 (Cambridge Univ. Press, 2021).
- Yuan, W. et al. Increased atmospheric vapor pressure deficit reduces global vegetation growth. *Sci. Adv.* **5**, eaax1396 (2019).
- Miralles, D. G., Gentile, P., Seneviratne, S. I. & Teuling, A. J. Land-atmospheric feedbacks during droughts and heatwaves: state of the science and current challenges. *Ann. N. Y. Acad. Sci.* **1436**, 19–35 (2019).
- Ficklin, D. L. & Novick, K. A. Historic and projected changes in vapor pressure deficit suggest a continental-scale drying of the United States atmosphere. *J. Geophys. Res. Atm.* **122**, 2061–2079 (2017).
- Humphrey, V. et al. Soil moisture-atmosphere feedback dominates land carbon uptake variability. *Nature* **592**, 65–69 (2021).
- Fu, Z. et al. Atmospheric dryness reduces photosynthesis along a large range of soil water deficits. *Nat. Commun.* <https://doi.org/10.1038/s41467-022-28652-7> (2022).
- Breshears, D. D. et al. The critical amplifying role of increasing atmospheric moisture demand on tree mortality and regional die-off. *Front. Plant Sci.* **4**, 266 (2013).
- Clarke, H. et al. Forest fire threatens global carbon sinks and population centres under rising atmospheric water demand. *Nat. Commun.* <https://doi.org/10.1038/s41467-022-34966-3> (2022).
- Büntgen, U. et al. Recent European drought extremes beyond Common Era background variability. *Nat. Geosci.* <https://doi.org/10.1038/s41561-021-00698-0> (2021).
- Treydte, K. et al. Signal strength and climate calibration in a European tree-ring isotope network. *Geophys. Res. Lett.* **34**, L24302 (2007).
- Treydte, K. et al. Impact of climate and CO₂ on a millennium-long tree-ring carbon isotope record. *Geochim. Cosmochim. Acta* **73**, 4635–4647 (2009).
- McCarroll, D. et al. Correction of tree ring stable carbon isotope chronologies for changes in the carbon dioxide content of the atmosphere. *Geochim. Cosmochim. Acta* **73**, 1539–1547 (2009).
- Klesse, S. et al. Oxygen isotopes in tree rings are less sensitive to tree size and stand dynamics than carbon isotopes. *Plant Cell Environ.* **41**, 2899–2914 (2018).
- Young, G. H. F. et al. Age trends in tree ring growth and isotopic archives: a case study of *Pinus sylvestris* L. from northwestern Norway. *Glob. Biogeochem. Cycles* <https://doi.org/10.1029/2010GB003913> (2011).
- Duffy, J. E. et al. Absence of age-related trends in stable oxygen isotope ratios from oak tree rings. *Glob. Biogeochem. Cycles* **33**, 841–848 (2019).
- Büntgen, U. et al. No evidence of age trends in oak stable isotopes. *Paleoceanogr. Paleoclimatol.* <https://doi.org/10.1029/2019PA003831> (2020).
- Gessler, A. et al. Stable isotopes in tree rings—toward a mechanistic understanding of isotope fractionation and mixing processes from the leaves to the wood. *Tree Physiol.* <https://doi.org/10.1093/treephys/tpu040> (2014).

24. Treydte, K. et al. Seasonal transfer of oxygen isotopes from precipitation and soil to the tree ring: Source water versus leaf water enrichment. *N. Phytol.* **202**, 772–783 (2014).
25. Sternberg, L., Pinzon, M. C., Anderson, W. T. & Jahren, A. H. Variation in oxygen isotope fractionation during cellulose synthesis: intramolecular and biosynthetic effects. *Plant Cell Environ.* **29**, 1881–1889 (2006).
26. Martínez-Sancho, E. et al. Unenriched xylem water contribution to cellulose synthesis influenced by atmospheric demand governs the intra-annual tree-ring $d^{18}O$ signature. *New Phyt.* **240**, 1743–1757 (2023).
27. Levesque, M. et al. Tree-ring isotopes capture interannual vegetation productivity dynamics at the biome scale. *Nat. Commun.* **10**, 742 (2019).
28. Daux, V. et al. Comparisons of the performance of $\delta^{13}C$ and $\delta^{18}O$ of *Fagus sylvatica*, *Pinus sylvestris*, and *Quercus petraea* in the record of past climate variations. *J. Geophys. Res. Biogeosci.* **123**, 1145–1160 (2018).
29. Vitali, V. et al. High-frequency stable isotope signals in uneven-aged forests as proxy for physiological responses to climate in Western Europe. *Tree Physiol.* **41**, 2046–2062 (2021).
30. Naulier, M. et al. A millennial summer temperature reconstruction for northeastern Canada using oxygen isotopes in subfossil trees. *Clim. Past* **11**, 1153–1164 (2015).
31. Field, R. D. et al. Tree-ring cellulose $\delta^{18}O$ records similar large-scale climate influences as precipitation $\delta^{18}O$ in the Northwest Territories of Canada. *Clim. Dyn.* **58**, 759–776 (2022).
32. Padrón, R. S. et al. Observed changes in dry-season water availability attributed to human-induced climate change. *Nat. Geosci.* **13**, 477–481 (2020).
33. Eyring, V. et al. Overview of the Coupled Model Intercomparison Project Phase 6 (CMIP6) experimental design and organization. *Geosci. Model Dev.* **9**, 1937–1958 (2016).
34. Dorado-Liñán, I. et al. Jet stream position explains regional anomalies in European beech forest productivity and tree growth. *Nat. Commun.* **13**, 2015 (2022).
35. Trouet, V., Babst, F. & Meko, M. Recent enhanced high-summer North Atlantic Jet variability emerges from three-century context. *Nat. Commun.* **9**, 180 (2018).
36. Luterbacher, J., Dietrich, D., Xoplaki, E., Grosjean, M. & Wanner, H. European seasonal and annual temperature variability, trends, and extremes since 1500. *Science* **303**, 1499–1503 (2004).
37. Derham, W. The history of the great frost in the last winter 1703 and 1708/9. *Phil. Trans.* **26**, 454–478 (1709).
38. Vicente-Serrano, S. M. et al. Recent changes of relative humidity: regional connections with land and ocean processes. *Earth Syst. Dyn.* **9**, 915–937 (2018).
39. Sherwood, S. & Fu, Q. A drier future? *Science* **343**, 737–739 (2014).
40. McDowell, N. G. et al. Mechanisms of woody-plant mortality under rising drought, CO_2 and vapour pressure deficit. *Nat. Rev. Earth Environ.* <https://doi.org/10.1038/s43017-022-00272-1> (2022).
41. Still, C. J. et al. No evidence of canopy-scale leaf thermoregulation to cool leaves below air temperature across a range of forest ecosystems. *Proc. Natl Acad. Sci. USA* <https://doi.org/10.1073/pnas.2205682119> (2022).
42. Lansu, E. M., van Heerwaarden, C. C., Stegehuis, A. I. & Teuling, A. J. Atmospheric aridity and apparent soil moisture drought in European forests during heat waves. *Geophys. Res. Lett.* **47**, e2020GL087091 (2020).
43. Zhao, M., Geruo, A., Liu, Y. & Kronings, A. G. Evapotranspiration frequently increases during droughts. *Nat. Clim. Change* **12**, 1024–1030 (2022).
44. Vicente-Serrano, S. M., McVicar, T. R., Miralles, D. G., Yang, Y. & Tomas-Burguera, M. Unraveling the influence of atmospheric evaporative demand on drought and its response to climate change. *Wiley Interdiscip. Rev. Clim. Change* <https://doi.org/10.1002/wcc.632> (2020).
45. Li, S. et al. Attribution of global evapotranspiration trends based on the Budyko framework. *Hydrol. Earth Syst. Sci.* **26**, 3691–3707 (2022).
46. Novick, K. A. et al. The increasing importance of atmospheric demand for ecosystem water and carbon fluxes. *Nat. Clim. Change* **6**, 1023 (2016).
47. Babst, F. et al. Twentieth century redistribution in climatic drivers of global tree growth. *Sci. Adv.* **5**, eaat4313 (2019).
48. Trotsiuk, V. et al. Tree growth in Switzerland is increasingly constrained by rising evaporative demand. *J. Ecol.* **109**, 2981–2990 (2021).
49. Zhang, Q. et al. Response of ecosystem intrinsic water use efficiency and gross primary productivity to rising vapor pressure deficit. *Environ. Res. Lett.* **14**, 074023 (2019).
50. Allen, C. D., Breshears, D. D. & McDowell, N. G. On underestimation of global vulnerability to tree mortality and forest die-off from hotter drought in the Anthropocene. *Ecosphere* **6**, 1–55 (2015).
51. de Dios, V. R. et al. Climate change induced declines in fuel moisture may turn currently fire-free Pyrenean mountain forests into fire-prone ecosystems. *STOTEN* **797**, 149104 (2021).

Publisher's note Springer Nature remains neutral with regard to jurisdictional claims in published maps and institutional affiliations.

Springer Nature or its licensor (e.g. a society or other partner) holds exclusive rights to this article under a publishing agreement with the author(s) or other rightsholder(s); author self-archiving of the accepted manuscript version of this article is solely governed by the terms of such publishing agreement and applicable law.

© The Author(s), under exclusive licence to Springer Nature Limited 2023

Kerstin Treydte ^{1,2} , **Laibao Liu** ^{3,5,7}, **Ryan S. Padrón**^{3,4,5,7}, **Elisabet Martínez-Sancho** ^{1,5,5,7}, **Flurin Babst** ⁶, **David C. Frank**⁷, **Arthur Gessler** ^{1,8}, **Ansgar Kahmen**⁹, **Benjamin Poulter** ¹⁰, **Sonia I. Seneviratne** ³, **Annemiek I. Stegehuis** ¹¹, **Rob Wilson**^{12,13}, **Laia Andreu-Hayles** ^{13,14,15}, **Roderick Bale** ¹⁶, **Zdzislaw Bednarz**¹⁷, **Tatjana Boettger**¹⁸, **Frank Berninger**¹⁹, **Ulf Büntgen**^{20,21,22}, **Valerie Daux** ²³, **Isabel Dorado-Liñán** ²⁴, **Jan Esper** ^{21,25}, **Michael Friedrich** ²⁶, **Mary Gagen**^{27,28}, **Michael Grabner** ²⁹, **Håkan Grudd** ³⁰, **Björn E. Gunnarsson**³¹, **Emilia Gutiérrez**⁵, **Polona Hafner** ³², **Marika Haupt**³³, **Emmi Hilasvuori**³⁴, **Ingo Heinrich** ³⁵, **Gerhard Helle** ³⁶, **Risto Jalkanen** ³⁷, **Högne Jungner**³⁸, **Maarit Kalela-Brundin**³⁹, **Andreas Kessler** ⁴⁰, **Andreas Kirchhefer** ⁴¹, **Stephan Klesse** ¹, **Marek Krapiec** ⁴², **Tom Levanič** ^{32,43}, **Markus Leuenberger**⁴⁴, **Hans W. Linderholm** ⁴⁵, **Danny McCarroll**²⁷, **Valérie Masson-Delmotte**²³, **Slawomira Pawelczyk** ⁴⁶, **Anna Pazdur**⁴⁶, **Octavi Planells**⁵, **Rutile Pukiene** ⁴⁷, **Katja T. Rinne-Garmston**³⁴, **Iain Robertson** ²⁷, **Antonio Saracino** ⁴⁸, **Matthias Saurer** ¹, **Gerhard H. Schleser**⁴⁹,

Kristina Seftigen⁴⁵, Rolf T. W. Siegwolf¹, Eloni Sonninen³⁸, Michel Stievenard²³, Elzbieta Szychowska-Krapiec⁴², Malgorzata Szymaszek⁵⁰, Luigi Todaro⁵¹, John S. Waterhouse⁵², Martin Weigl-Kuska⁵³, Rosemarie B. Weigt^{1,54}, Rupert Wimmer²⁹, Ewan J. Woodley⁵⁵, Adomas Vitas⁵⁶, Giles Young³⁴ & Neil J. Loader²⁷

¹Research Unit Forest Dynamics, Swiss Federal Institute for Forest, Snow and Landscape Research WSL, Birmensdorf, Switzerland. ²Oeschger Centre for Climate Change Research, University of Bern, Bern, Switzerland. ³Institute for Atmospheric and Climate Science, ETH Zurich, Zurich, Switzerland. ⁴Research Unit Mountain Hydrology and Mass Movements, Swiss Federal Institute for Forest, Snow and Landscape Research WSL, Birmensdorf, Switzerland. ⁵Department of Biological Evolution, Ecology and Environmental Sciences, University of Barcelona, Barcelona, Spain. ⁶School of Natural Resources and the Environment, University of Arizona, Tucson, AZ, USA. ⁷Laboratory of Tree Ring Research, University of Arizona, Tucson, AZ, USA. ⁸Department of Environmental Systems Sciences, ETH Zurich, Zurich, Switzerland. ⁹Department of Environmental Sciences – Botany, University of Basel, Basel, Switzerland. ¹⁰Earth Sciences Division, Biospheric Sciences Laboratory, NASA Goddard Space Flight Center, Greenbelt, MD, USA. ¹¹Laboratoire de Géologie, IPSL, CNRS UMR 8538, École Normale Supérieure, PSL University, Paris, France. ¹²School of Earth & Environmental Sciences, University of St. Andrews, Andrews, UK. ¹³Tree Ring Laboratory, Lamont-Doherty Earth Observatory, Columbia University, New York, NY, USA. ¹⁴Centre for Research on Ecology and Forestry Applications CREAM, Barcelona, Spain. ¹⁵ICREA, Barcelona, Spain. ¹⁶University of Wales Trinity Saint David, Swansea, UK. ¹⁷Department of Forest Biodiversity, Agricultural University, Krakow, Poland. ¹⁸Department of Catchment Hydrology, Helmholtz Centre for Environmental Research UFZ, Halle, Germany. ¹⁹Department of Forest Sciences, University of Helsinki, Helsinki, Finland. ²⁰Department of Geography, University of Cambridge, Cambridge, UK. ²¹Global Change Research Institute (CzechGlobe), Czech Academy of Sciences, Brno, Czech Republic. ²²Department of Geography, Faculty of Science, Masaryk University, Brno, Czech Republic. ²³Laboratoire des Sciences du Climat et de l'Environnement, UMR 8212 CEA-CNRS-UVSQ, Université Paris-Saclay & Institut Pierre Simon Laplace, Gif-sur-Yvette, France. ²⁴Systems and Natural Resources Department, Universidad Politécnica de Madrid, Madrid, Spain. ²⁵Department of Geography, Johannes-Gutenberg University, Mainz, Germany. ²⁶University of Hohenheim, Hohenheim Gardens, Stuttgart, Germany. ²⁷Department of Geography, Swansea University, Swansea, UK. ²⁸WWF-UK, Surrey, UK. ²⁹Institute of Wood Technology and Renewable Resources, University of Natural Resources and Life Sciences BOKU Vienna, Tulln, Austria. ³⁰Swedish Polar Research Secretariat, Abisko Scientific Research Station, Abisko, Sweden. ³¹Stockholm Tree Ring Laboratory, Department of Physical Geography, Stockholm University, Stockholm, Sweden. ³²Department of Yield and Silviculture, Slovenian Forestry Institute, Ljubljana, Slovenia. ³³Department of Isotope Hydrology, Helmholtz Centre for Environmental Research UFZ, Halle, Germany. ³⁴Natural Resources Institute Finland (Luke), Helsinki, Finland. ³⁵Deutsches Archäologisches Institut Berlin, Berlin, Germany. ³⁶Section 4.3 Climate Dynamics and Landscape Evolution, German Research Centre for Geosciences GFZ, Potsdam, Germany. ³⁷Silva Lapponica, Rovaniemi, Finland. ³⁸Laboratory of Chronology, University of Helsinki, Helsinki, Finland. ³⁹Forestry Museum, Lycksele, Sweden. ⁴⁰Derivative Infrastructure & Analytics – Architecture, Bank Vontobel AG, Zürich, Switzerland. ⁴¹Dendroökologen, Tromsø, Norway. ⁴²Faculty of Geology, Geophysics and Environmental Protection, AGH University of Science and Technology, Krakow, Poland. ⁴³Faculty of Mathematics, Natural Sciences and Information Technologies, University of Primorska, Koper, Slovenia. ⁴⁴Climate and Environmental Physics Division and Oeschger Centre for Climate Change Research, University of Bern, Bern, Switzerland. ⁴⁵Department of Earth Sciences, University of Gothenburg, Gothenburg, Sweden. ⁴⁶Division of Geochronology and Environmental isotopes, Institute of Physics – CSE, Silesian University of Technology, 44-100, Gliwice, Poland. ⁴⁷The State Scientific Research Institute Nature Research Centre, Vilnius, Lithuania. ⁴⁸Department of Agricultural Sciences, University of Naples Federico II, Portici-Napoli, Italy. ⁴⁹Institute of Bio- and Geosciences Agrosphere (IBG-3), Research Centre Jülich GmbH, Jülich, Germany. ⁵⁰Academic Secondary School, Gliwice, Poland. ⁵¹School of Agriculture, Forest, Food and Environmental Sciences (SAFE), University of Basilicata I-85100, Potenza, Italy. ⁵²School of Life Sciences, Anglia Ruskin University, Cambridge, UK. ⁵³Austrian Forest Products Research Society, Vienna, Austria. ⁵⁴Laboratory of Atmospheric Chemistry, Paul Scherrer Institute, Villigen, Switzerland. ⁵⁵Department of Geography, Faculty of Environment, Science and Economy, University of Exeter, Exeter, UK. ⁵⁶Vytautas Magnus University, Kaunas, Lithuania. ⁵⁷These authors contributed equally: Laibao Liu, Ryan S. Padrón, Elisabet Martínez-Sancho ✉e-mail: kerstin.treydte@wsl.ch

Methods

European network of tree-ring $\delta^{18}\text{O}$ records

A network of 45 sites with tree-ring cellulose $\delta^{18}\text{O}$ chronologies across Europe was established (Supplementary Table 1) using data primarily from the two EU-funded projects ISONET (20 sites) and Millennium (15 sites), and the Swiss Sinergia project iTREE (6 sites). Four additional data sets were downloaded from the NOAA paleoclimate database ('Ang' and 'Fon'⁵², 'Ger'⁵³, 'Cze'¹⁵).

The sampling design considered temperate lowland sites, with tree growth governed by a complex combination of environmental factors and also ecologically extreme high-elevation sites where few climatic factors dominate tree growth¹⁶ (Extended Data Table 1). Sites range from 5 to 2200 m elevation, with the majority situated in two elevation bands: 0–500 m and 1500–2200 m. High-altitude sites are concentrated in the south of the network. The network is dominated by oak and pine species (16 and 17 sites respectively), but also contains 5 spruce, 3 beech, 2 larch, 1 juniper and 1 cedar site (Supplementary Table 1). At each location the most abundant and long-lived trees were selected and at least four dominant trees per site were used for stable isotope analysis (1–2 cores per tree). In general, oak $\delta^{18}\text{O}$ measurements were performed on latewood (except CAV, where no separation in early and latewood was possible owing to particularly narrow rings), while whole rings were analysed for beech and conifers (Supplementary Information).

Tree-ring widths were measured and cross-dated following standard procedures to ensure correct dating of each annual ring. Individual rings were separated with a scalpel under a microscope. At some sites, tree rings from the same year were pooled prior to cellulose extraction, while at others individual trees were measured and averaged to site chronologies. For iTREE, 5–7 dominant and 5 suppressed trees were analysed at each site¹⁹, but for consistency with other sites, we developed chronologies using the dominant trees only. Cellulose was extracted using standard techniques⁵⁴. Oxygen isotope analysis was conducted on CO obtained from pyrolysing the samples in elemental analysers and measurements with isotope-ratio mass spectrometry⁵⁴. Isotope values are given as δ -values calculated from the isotope ratios $^{18}\text{O}/^{16}\text{O}$ (=R) as $\delta^{18}\text{O} = (\text{R}_{\text{sample}}/\text{R}_{\text{standard}} - 1) * 1000 \text{‰}$ (referring to the international standard VSMOW) and have a long-term estimated methodological error of $<0.2 \text{‰}$. The lengths of the chronologies varied from 95 years ('Tur' and 'San') to 1500 years ('Cze') with a median chronology length of 288 years. Our study was restricted to the past 415 years, back to 1600 CE.

Four datasets were downloaded from the NOAA Paleoclimatology database, that is, two French chronologies⁵², one of them Fontainebleau (Fon) replacing and extending the previous chronology established in ISONET, and Angoulême (Ang). The Fon chronology, provided as $\delta^{18}\text{O}$ anomalies only, was scaled to the 20th century mean of the previous Fon chronology, and Ang was scaled to the mean of the old trees at this site⁵². For the Spanish dataset Gerber (Ger)⁵³ the mean was calculated of all five individual tree series, even though the mean inter-series correlation was relatively low (mean $r_{1901-2009} = 0.22$). For 'Cze'¹⁵ all $\delta^{18}\text{O}$ data were selected that reach back to 1600 CE, including living trees and relict wood from several locations in the Czech Republic. Due to offsets between individual measurements, the chronology was generated by calculating anomalies from the mean of each individual data set and averaging them after.

All site $\delta^{18}\text{O}$ records were screened for missing values and gaps filled based on information from adjacent chronologies using the software program ARSTAN⁵⁵. Furthermore, all chronologies were tested for potential artificial, non-climatic long-term trends for example possibly caused by pooling multiple trees. The general absence of such trends (except the early portions of Col, Ser, and Ped, which did not reach 75% membership component during fuzzy cluster analysis, see below) is in line with other studies^{20–22} and allowed for further analyses using the non-detrended data.

Spatial clustering and regional principal components

Fuzzy cluster analysis^{56,57} was applied for the period 1920–1994 CE on the raw tree-ring $\delta^{18}\text{O}$ chronologies with the aim to identify regional groups across the network. Contrary to hard clustering, fuzzy clustering allows data to belong to more than one cluster with membership grades assigned to each of the data points. These membership grades indicate the degree to which data belong to each cluster. The number of clusters is defined by maximizing the correlation between sites within each cluster over the 1920–2000 period. The best correlation was obtained with five clusters representing distinct geographic regions (A&P, WE, ECE, SF and NF). The membership exponent (membership in %) was used to identify the strength of contribution of the individual site chronologies to the common variance of the cluster. Only site chronologies exceeding a membership exponent threshold of 75% were selected for the development of regional time series for climate reconstruction (Extended Data Fig. 5).

To create such regional time series, we applied nested principal component analysis⁵⁸ for each cluster separately. Since the number of available chronologies decreases back in time, all tree-ring $\delta^{18}\text{O}$ predictors within a given time period were used to generate a principal component regression model, then the shortest chronologies were removed and another model was generated with the remaining chronologies. This nesting approach was repeated back in time and resulted in a varying number of 'nests' per cluster back through time (Supplementary Table 2). The first principal component (PC1) was calculated for each cluster and the PC1 factors of the individual nests per cluster spliced together after scaling to VPD. The variance explained by PC1 of the individual nests varied between 46% and 61% for western Europe (five nests), between 62% and 64% for eastern central Europe (four nests), between 58% and 61% for the Alps & Pyrenees (five nests), between 55% and 62% for southern Fennoscandia (four nests), and between 38% and 45% for northern Fennoscandia (three nests).

Calibration, verification and VPD reconstruction

After confirmation of normal distribution of the raw tree-ring $\delta^{18}\text{O}$ data as well as the PC1 nests by the Shapiro normality test, Pearson's correlation coefficients between tree-ring $\delta^{18}\text{O}$ records and climate variables were calculated. This was done for each individual raw site $\delta^{18}\text{O}$ chronology on a site-by-site basis as well as for each of the nested PC1 records developed for the five regional clusters using the $0.5^\circ \times 0.5^\circ$ monthly gridded meteorological dataset of the Climate Research Unit, University of East Anglia, UK (CRU TS4.05)⁵⁹. Analyses considered 11 monthly variables, that is, mean (T_{mean}), minimum (T_{min}) and maximum (T_{max}) temperatures, precipitation sums (PPT), standardized precipitation evapotranspiration indices (SPEI), cloud cover (CLD), wet day frequencies (WET), potential evapotranspiration (PET), vapor pressure (VP), water balance (WAB, calculated as precipitation minus potential evapotranspiration) and, most importantly, atmospheric vapor pressure deficit (VPD). VPD was calculated as saturated minus actual vapor pressure with the latter available as a standard CRU dataset, whereas the former was derived from CRU T_{mean} data using the formula $\text{VP}_{\text{sat}} = 6.11 * 10^{(7.5 * T) / (237.3 + T)}$ ⁶⁰.

The period 1920–2000 was defined as the core period for calibration due to some irregularities in the available climate data prior to 1920 (for example, abrupt changes in magnitude or variance) and reduced replication of the composite $\delta^{18}\text{O}$ records in the most recent period. In a first step, monthly correlations were calculated from March of the year before tree-ring formation to October of the year of tree-ring formation and for 186 combinations of months using the closest gridpoint to identify the seasonality in the climate response at each site. Calculations were performed in R using the python module rpy2 (R version 3.5.1, Python version 3.7., rpy2 version 2.9.5) (<https://rpy2.github.io>).

Spatial correlation fields for each of the five sub-regions were calculated based on the gridded VPD dataset of June to August (JJA). All VPD gridpoints revealing significance of the correlation coefficients

at $P < 0.001$ with the corresponding regional PC1 record were averaged and this mean used as target for climate reconstruction prior to the instrumental period.

Calibration/verification statistics such as explained variance (R^2), reduction of error (RE), coefficient of efficiency (CE) and Durbin-Watson test (DW) were applied to each individual PC1 nest to quantify the signal strength and the temporal robustness of the reconstructions. The goodness of the fit between the PC1 records of the different sub-regions and regional summer VPD was assessed by correlation, comparing the linear trends of the regression residuals and the Durbin-Watson statistic – a measure of the persistence in the residuals of a regression (between proxy and station data) (Supplementary Table 2). Variability of summer VPD prior to the instrumental period was reconstructed by scaling each spliced regional PC1 nest to the same mean and variance as its corresponding VPD observational record over the full 1920–2000 calibration period.

VPD simulations from Earth system models

The monthly data output from twelve Earth system models (ESMs) from the sixth phase of the Coupled Model Intercomparison Project (CMIP6)³³ with extracted data corresponding to the spatial coverage of our reconstructions plus observations were utilized for simulations of summer VPD: ACCESS-ESM1-5, CESM2, CMCC-ESM2, CNRM-ESM2-1, CanESM5, EC-Earth3-Veg, GFDL-ESM4, IPSL-CM6A-LR, MIROC-ES2L, MPI-ESM1-2-LR, MRI-ESM2-0, and UKESM1-0-LL. The model selection was based on the availability of the required output variables of temperature and relative humidity for the different types of simulations used in our study. Only one model version per model family was selected to avoid biasing the multi-model mean to those model families with more versions available.

Three main types of simulations were considered for the analyses: ‘piControl’, ‘historical’ and ‘ssp245’, while using one ensemble member per model. The ‘piControl’ scenario was used to estimate natural climate variability with simulations including external natural forcing (that is, volcanic eruptions, solar irradiance variability) while keeping anthropogenic forcing constant (that is, human-induced changes to CO₂ concentration, aerosols, land use etc.) at pre-industrial conditions. In contrast, ‘historical’ simulations (1850–2014) include both natural and anthropogenic radiative forcing. For the analyses with respect to the period 1991–2020, we combined the ‘historical’ simulations extending until 2014 with simulations from the ‘ssp245’ scenario during 2015 to 2020, an intermediate scenario that is closest to emissions implied by current policies. Furthermore, we conducted additional tests using ‘hist-nat’ simulations including historical (1850–2020) natural forcing and excluding anthropogenic forcing (Supplementary Table 4), as well as ‘hist-noLu’ simulations which are similar to the ‘historical’ simulations but keep land use/land cover constant at pre-industrial conditions (Supplementary Table 6, Supplementary Information).

As for the observations, VPD was calculated as saturated minus actual vapor pressure: $VPD_{\text{sat}} = 6.11 \cdot 10^4 \cdot ((7.5 \cdot T)/(237.3 + T))$; $VPD_{\text{act}} = VPD_{\text{sat}} \cdot \text{relative humidity}/100$. For these calculations near-surface air temperature and relative humidity were used from all models. For each year the average of the 3-month period June–August was computed. All estimates were first computed for each CMIP6 ESM at every grid cell ($\sim 2^\circ \times 2^\circ$ depending on each model) and were then area-weighted averaged to the same regional scale of the corresponding reconstructions. Time series of normalized VPD are shown in Supplementary Fig. 3 and the interannual variability from the ‘piControl’ simulations are provided in Supplementary Table 5. We note that the interannual variability of the reconstruction during 1600 to 1849 is generally lower than that of the ESMs across all four analysed regions.

Attribution of VPD to human-induced climate change

To assess the human-induced climate change effects^{32,61} on the observed summer VPD from 1991 to 2020, we compared it to the expected VPD

from natural climate variability under pre-industrial atmospheric CO₂ conditions. To do so, we estimated an empirical distribution of 30-year mean VPD arising from natural climate variability by randomly sampling (without repeating years) 500 different 30-year subsets from the reconstruction between 1600 and 1850. In addition, we estimated the expected summer VPD from 1991 to 2020 based on historical ESM simulations with human-induced plus natural radiative forcing (combination of ‘historical’ and ‘ssp245’ type simulations), as well as the natural climate variability VPD distribution based on simulations with pre-industrial atmospheric forcing (‘piControl’ type simulations). To estimate the VPD variability from the piControl 500-year simulations we also randomly sampled (without repeating years) 500 different 30-year subsets. To allow comparability between the reconstruction and the ESMs, VPD was normalized by subtracting the mean and dividing by the interannual standard deviation of the entire pre-industrial period. As additional tests we also estimated recent summer VPD from simulations excluding anthropogenic forcing (‘hist-nat’) and from simulations with land use/land cover kept constant at pre-industrial conditions (‘hist-noLu’).

Data availability

All raw tree-ring $\delta^{18}\text{O}$ chronologies used in this study together with the final summer VPD reconstructions can be downloaded at the NOAA National Centre for Environmental Information (NCEI): <https://www.ncei.noaa.gov/access/paleo-search/study/38660>.

The CMIP6 data used in this study are available at <https://esgf-node.lln.gov/search/cmip6/>. Detailed inputs for the search query are as follows: source IDs are ACCESS-ESM1-5, CESM2, CMCC-ESM2, CNRM-ESM2-1, CanESM5, EC-Earth3-Veg, GFDL-ESM4, IPSL-CM6A-LR, MIROC-ES2L, MPI-ESM1-2-LR, MRI-ESM2-0, and UKESM1-0-LL; experiment IDs are piControl, historical and ssp245, also hist-nat and hist-noLu; variant label is r1i1p1f1 or the next lowest number if unavailable for some models; frequency is mon; and variables are tas and hurs.

Code availability

R-codes used for fuzzy cluster and principal component analysis are available at https://github.com/Treydte/code_NGeo23, and python-codes for site-based monthly and seasonal correlations with climate variables are available at <https://github.com/andreasessler/VPDSeasonalCorr>.

References

- Labuhn, I. et al. French summer droughts since 1326 CE: a reconstruction based on tree ring cellulose. *Clim. Past* **12**, 1101–1117 (2016).
- Konter, O. et al. Climate sensitivity and parameter coherency in annually resolved $\delta^{13}\text{C}$ and $\delta^{18}\text{O}$ from *Pinus uncinata* tree-ring data in the Spanish Pyrenees. *Chem. Geol.* **377**, 12–19 (2014).
- Boettger, T. et al. Wood cellulose preparation methods and mass spectrometric analyses of $\delta^{13}\text{C}$, $\delta^{18}\text{O}$, and nonexchangeable $\delta^2\text{H}$ values in cellulose, sugar, and starch: an interlaboratory comparison. *Anal. Chem.* **79**, 4603–4612 (2007).
- Cook, E. R., Krusic, P. J., Peters, K. & Holmes, R. L. Program ARSTAN (version 49v1_Mac), autoregressive tree-ring standardization program (Tree-Ring Laboratory of Lamont-Doherty Earth Observatory, 2017).
- Maechler, M., Rousseeuw, P., Struyf, A., Hubert, M. & Hornik, K. cluster: Cluster Analysis Basics and Extensions. R package version 2.1.3 <https://CRAN.R-project.org/package=cluster> (2022).
- Kaufman, L., & Rousseeuw, P. J. *Finding Groups in Data—An Introduction to Cluster Analysis* (Wiley, 1990); <https://doi.org/10.1002/9780470316801>
- Frank, D. C. & Esper, J. Temperature reconstructions and comparisons with instrumental data from a tree-ring network for the European Alps. *Int. J. Clim.* **25**, 1437–1454 (2005).

59. Harris, I. et al. Version 4 of the CRU TS monthly high-resolution gridded multivariate climate dataset. *Sci. Data* **7**, 109 (2020).
60. Murray, F. W. On the computation of saturation vapor pressure. *J. Appl. Meteorol.* **6**, 203–204 (1967).
61. Grant, L. et al. Attribution of global lake systems change to anthropogenic forcing. *Nat. Geosci.* **14**, 849–854 (2021).

Acknowledgements

We acknowledge the World Climate Research Programme's Working Group on Coupled Modelling, which is responsible for the Coupled Model Intercomparison Project (CMIP), and we thank the climate modeling groups for producing their model output and making it available. For the CMIP, the US Department of Energy's Program for Climate Model Diagnosis and Intercomparison provides coordinating support and led development of the software infrastructure in partnership with the Global Organization for Earth System Science Portals.

This study was funded by the EC projects ISONET EVK2-CT-2002-00147 and Millennium FP6-2004-GLOBAL-017008-2 and by the Swiss National Science Foundation (SNSF) projects iTREE CRSII3_136295 and TROXY 200021_175888. Other funding included ERC 724750 (AK), NASA's Terrestrial Ecology programme (BP), Slovenian Research Agency P4-0107 (TL, PH), MIUR-PRIN 2002 2002075152 & MIUR-PRIN 2005 2005072877 (AS, LT), PALEOMEX-ISOMEX programme CNRS-INSU (VD), Fundació La Caixa through the Junior Leader Program LCF/BQ/LR18/11640004 (IDL), ERC 755865 & Academy of Finland 295319 and 343059 (KR-G), Czech Science Foundation CZ.02.1.01/0.0/0.0/16_019/0000797 (UB, JE), Spanish Ministry of Science and Technology REN2002-11476-E/CLI (EG), and ERC AdG 882727 (JE), UKRI EP/X025098/1 (NJL). L.L., R.P., and S.I.S. acknowledge support from the European Union's Horizon 2020 Research and Innovation programme (grant agreement 821003 (4C)). The views and conclusions contained in this document are

those of the authors and should not be interpreted as representing the opinions or policies of the funding agencies and supporting institutions.

Author contributions

K.T., L.L., R.P., F.B., D.C.F., A. Kahmen, S.I.S. and N.J.L. designed the research; K.T., L.L., R.P., F.B., D.C.F., E.M.-S., B.P. and R.W. performed the research with input from A.G., A. Kahmen, A. Kessler, A.I.S. and S.I.S. K.T. wrote the paper. All listed authors from L.A.-H. to G.Y. were involved in data production and provided feedback on the manuscript.

Competing interests

The authors declare no competing interests.

Additional information

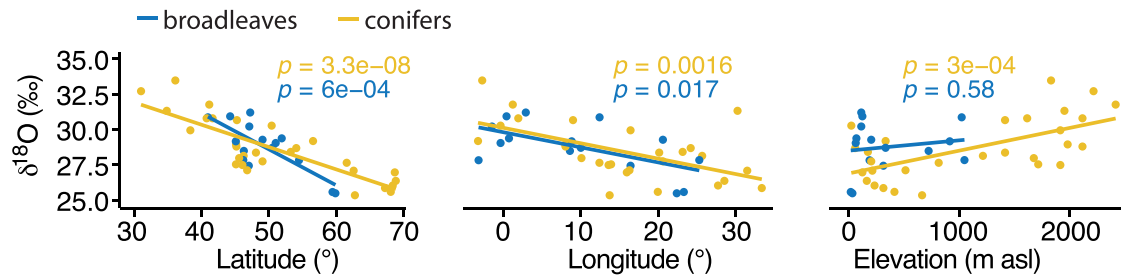
Extended data is available for this paper at <https://doi.org/10.1038/s41561-023-01335-8>.

Supplementary information The online version contains supplementary material available at <https://doi.org/10.1038/s41561-023-01335-8>.

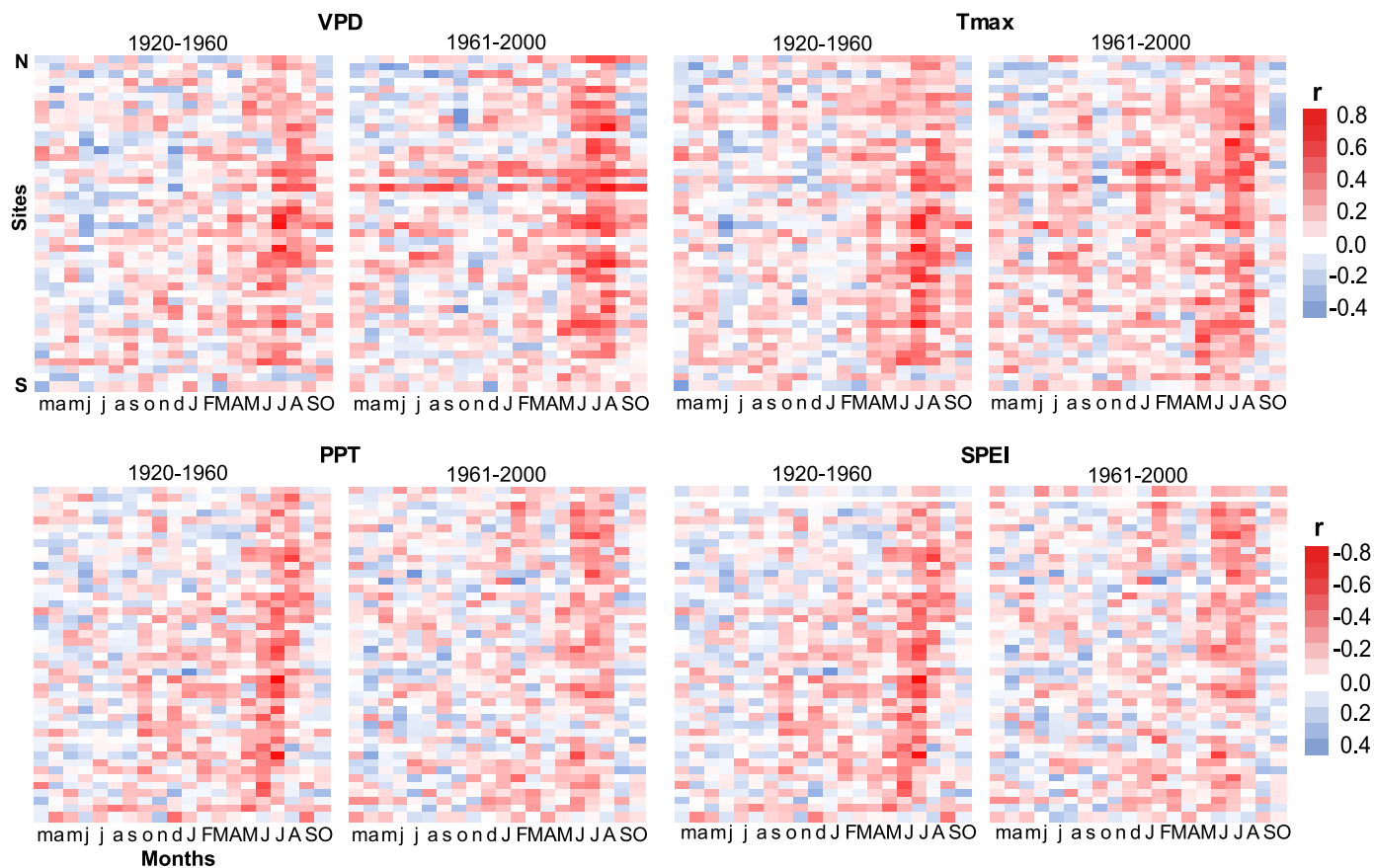
Correspondence and requests for materials should be addressed to Kerstin Treydte.

Peer review information *Nature Geoscience* thanks William Lukens, Christopher Still and the other, anonymous, reviewer(s) for their contribution to the peer review of this work. Primary Handling Editor: James Super, in collaboration with the *Nature Geoscience* team.

Reprints and permissions information is available at www.nature.com/reprints.

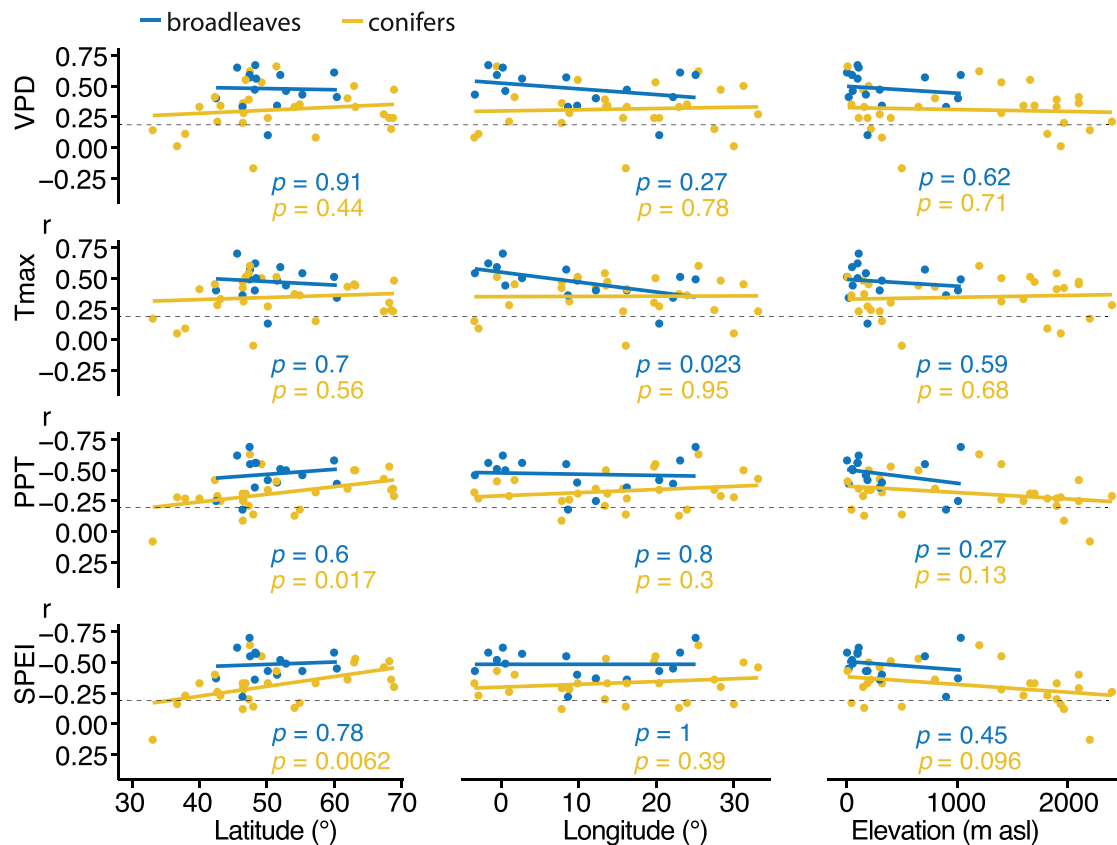


Extended Data Fig. 1 | Dependency of mean $\delta^{18}\text{O}$ site values of the common period 1900-1994 on geographic location. p-values below 0.05 indicate significant relationships.



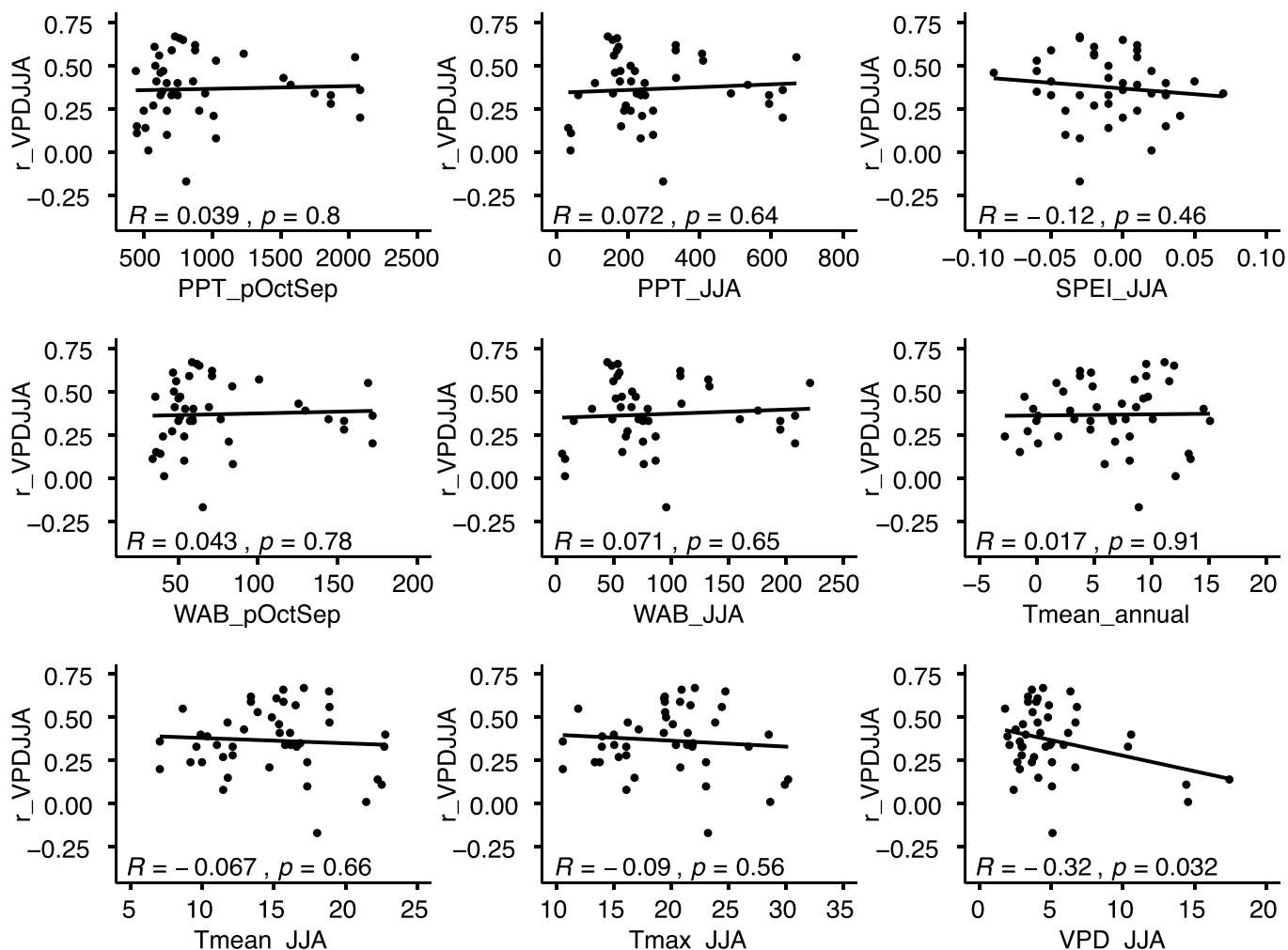
Extended Data Fig. 2 | Climate sensitivity of the site tree-ring $\delta^{18}\text{O}$ chronologies in two independent time periods. Periods cover 1920-1960 and 1961-2000; shorter for those records that end in 1994, 1996 and 1998, (see Extended Data Table 1). Colours indicate Pearson's correlation coefficients calculated between each of the 45 site $\delta^{18}\text{O}$ chronologies of the network and the

closest gridpoints of VPD, maximum temperature (T_{max}), precipitation sums and SPEI for each individual month from March of the year before to October of the actual year of tree-ring formation. For VPD and T_{max} , red colours indicate positive correlations, for PPT and SPEI red colours indicate negative correlations. Order of sites from North to South corresponds to the order in Extended Data Table 1.



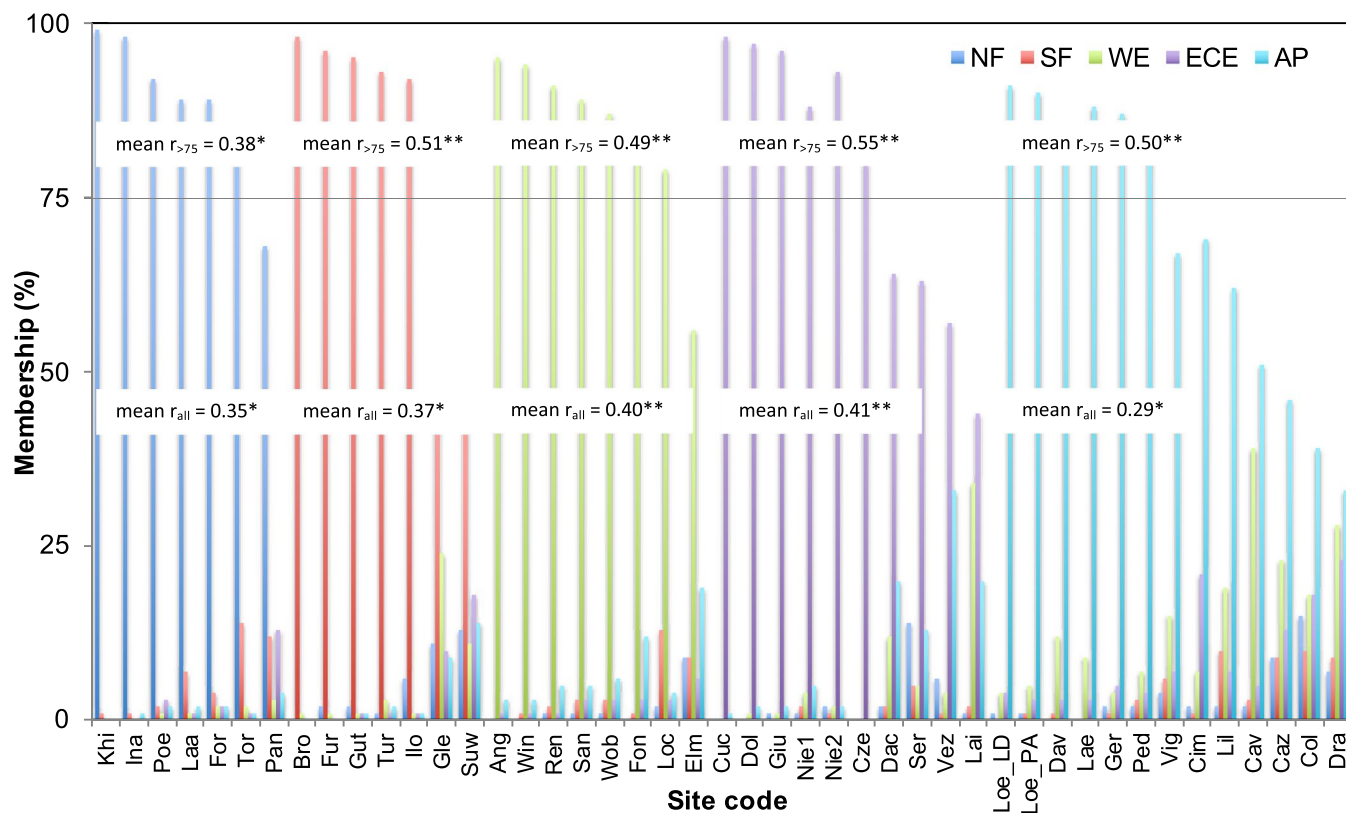
Extended Data Fig. 3 | Relationship between climate- $\delta^{18}\text{O}$ correlations and geographic location for VPD, T_{max} , precipitation (PPT) and SPEI in summer (June to August). Each point indicates a correlation coefficient calculated between a site $\delta^{18}\text{O}$ chronology and the closest gridpoint dataset, plotted as a function of latitude, longitude and elevation. Points above the dashed horizontal

line are significant at $P < 0.05$. p-values in the legend indicate the significance of the slope of the linear regression line. Most p-values are above 0.05 which suggests independency of the correlation strength from geographical location. Note the inverse y-axis for PPT and SPEI.



Extended Data Fig. 4 | Relationship between climate- $\delta^{18}\text{O}$ correlations and long-term means (period 1920-1994) of precipitation sums (PPT), SPEI, water balance (WAB), mean temperature (T_{mean}), maximum temperature (T_{max}) and VPD. Each point indicates a correlation coefficient calculated between a site $\delta^{18}\text{O}$ chronology and the closest gridpoint climate dataset,

plotted as a function of the nine selected climate long-term means ('climatic regions'). R - and p -values in the legend indicate the significance of the relationship. Most p -values are above 0.05 which suggests independency of the correlation strength from the climatic region.



Extended Data Fig. 5 | Contribution of the individual site chronologies to the common variance in the regional clusters of Northern Fennoscandia (NF), Southern Fennoscandia (SF), Western Europe (WE), Eastern Central Europe (ECE) and Alps & Pyrenees (AP). Membership (%) the contribution to the common variance in a cluster in percentage. Mean r_{all} is the mean inter-series correlation coefficient (that is, the common signal strength) of all chronologies

contributing to the corresponding cluster, mean $r_{>75}$ is the mean inter-series correlation of the chronologies with a membership >75% in a cluster (* $P < 0.01$, ** $P < 0.001$). Calculations are based on the period 1920-2000. Sites above a membership threshold of 75% (straight line) were used for the development of regional chronologies through nested principal component analysis. Site codes see Supplementary Table 1.

Extended Data Table 1 | European Network of tree-ring cellulose $\delta^{18}\text{O}$ chronologies listed from North to South

Country	Site name	Code	Lat.	Long.	Genus	Species	Elevation (m asl)	Start yr (CE)	End yr (CE)	Length (years)	$\delta^{18}\text{O}$ mean (‰) 1900-1994 CE
Finland	Inari	Ina*	68.93	28.32	<i>Pinus</i>	<i>sylvestris</i>	150	1600	2002	403	26.37
Norway	Forfjorddalen	For**	68.79	15.72	<i>Pinus</i>	<i>sylvestris</i>	110	1600	2001	402	26.97
Finland	Laanila	Laa**	68.50	27.50	<i>Pinus</i>	<i>sylvestris</i>	220	1620	2001	382	26.04
Sweden	Torneträsk	Tor	68.22	19.72	<i>Pinus</i>	<i>sylvestris</i>	400	1600	2008	409	25.59
Russia	Khibiny	Khi**	67.41	33.15	<i>Pinus</i>	<i>sylvestris</i>	300	1900	2005	106	25.86
Sweden	Furuberget	Fur**	63.16	13.50	<i>Pinus</i>	<i>sylvestris</i>	650	1736	2006	271	25.35
Finland	Ilomantsi	Ilo*	62.98	31.27	<i>Pinus</i>	<i>sylvestris</i>	200	1600	2002	403	27.09
Norway	Gutuli	Gut*	62.00	12.18	<i>Pinus</i>	<i>sylvestris</i>	800	1600	2003	404	27.65
Finland	Turku	Tur**	60.41	22.17	<i>Quercus</i>	<i>robur</i>	20	1900	1994	95	25.49
Finland	Bromarv	Bro*	60.00	23.08	<i>Quercus</i>	<i>robur</i>	5	1901	2002	102	25.58
UK	Glen Affric	Gle*	57.25	-3.50	<i>Pinus</i>	<i>sylvestris</i>	320	1650	2007	358	29.19
UK	Lochwood	Loc**	55.27	-3.43	<i>Quercus</i>	<i>robur</i>	175	1749	2003	255	27.83
Lithuania	Pane Silas	Pan*	54.88	23.97	<i>Pinus</i>	<i>sylvestris</i>	45	1816	2002	187	28.69
Poland	Suwalki	Suw*	54.10	22.93	<i>Pinus</i>	<i>sylvestris</i>	160	1600	2003	404	28.42
UK	Sandringham	San**	52.83	0.50	<i>Quercus</i>	<i>robur</i>	56	1900	1994	95	29.38
UK	Woburn	Wob*	51.98	-0.59	<i>Quercus</i>	<i>robur</i>	50	1604	2003	400	29.05
Germany	Dransfeld	Dra*	51.50	9.78	<i>Quercus</i>	<i>petraea</i>	320	1776	2003	228	28.71
UK	Windsor	Win*	51.41	-0.59	<i>Pinus</i>	<i>sylvestris</i>	10	1900	2003	104	30.28
Poland	Niopol Gibiel	Nie1*	50.12	20.38	<i>Pinus</i>	<i>sylvestris</i>	190	1900	2003	104	27.75
Poland	Niopol Gibiel	Nie2*	50.12	20.38	<i>Quercus</i>	<i>robur</i>	190	1627	2003	377	29.28
Slovakia	Hlina Dolina	Dol	49.19	19.90	<i>Picea</i>	<i>abies</i>	1400	1821	2012	192	28.37
Czech Rep.	various	Cze	var.	var.	<i>Quercus</i>	<i>spp.</i>	400	1600	2018	419	27.56
France	Fontainebleau	Fon**	48.38	2.67	<i>Quercus</i>	<i>petraea</i>	100	1600	2000	675	31.21
France	Rennes	Ren*	48.25	-1.70	<i>Quercus</i>	<i>robur</i>	100	1751	1998	248	30.22
Austria	Lainzer Tierg.	Lai*	48.18	16.20	<i>Quercus</i>	<i>petraea</i>	300	1600	2003	404	27.44
Austria	Poellau	Poe*	47.95	16.06	<i>Pinus</i>	<i>nigra</i>	500	1600	2002	403	27.12
Switzerland	Laegern	Lae	47.48	8.37	<i>Fagus</i>	<i>sylvatica</i>	709	1840	2012	174	28.49
Romania	Giumalau	Giu	47.45	25.45	<i>Picea</i>	<i>abies</i>	1200	1761	2013	253	28.14
Romania	Cucuraena	Cuc	47.40	25.08	<i>Fagus</i>	<i>sylvatica</i>	1033	1850	2013	164	27.84
Austria	Dachstein	Dac**	47.28	13.36	<i>Pinus</i>	<i>cembra</i>	1900	1900	1996	97	27.49
Switzerland	Davos	Dav	46.82	9.86	<i>Picea</i>	<i>abies</i>	1660	1853	2012	160	27.98
Switzerland	Vigera	Vig*	46.50	8.77	<i>Pinus</i>	<i>sylvestris</i>	1400	1675	2003	329	30.67
Switzerland	Loetschental	LoeLD**	46.43	7.80	<i>Larix</i>	<i>decidua</i>	2100	1600	2004	355	28.80
Switzerland	Loetschental	LoePA	46.39	7.77	<i>Picea</i>	<i>abies</i>	1966	1783	2012	230	28.95
Slovenia	Veza	Veza**	46.37	13.69	<i>Larix</i>	<i>decidua</i>	1700	1600	2006	407	27.54
Switzerland	Cavergno	Cav*	46.35	8.60	<i>Quercus</i>	<i>petraea</i>	900	1637	2002	366	29.17
France	Angouleme	Ang	45.55	0.18	<i>Quercus</i>	<i>robur</i>	110	1360	2004	645	30.94
Spain	Pinar de Lillo	Lil*	43.07	-5.25	<i>Pinus</i>	<i>sylvestris</i>	1600	1600	2002	403	30.80
Spain	Valle Gerber	Ger	42.60	0.99	<i>Pinus</i>	<i>uncinata</i>	2400	1901	2009	109	31.77
Italy	Monte Cimino	Cim	42.41	12.20	<i>Fagus</i>	<i>sylvatica</i>	1008	1870	2012	143	30.87
Spain	Pedraforca	Ped*	42.23	1.70	<i>Pinus</i>	<i>uncinata</i>	2100	1600	2003	404	30.80
Italy	Serra di Cris	Ser*	39.93	16.20	<i>Pinus</i>	<i>leucodermi</i>	1900	1604	2003	400	29.95
Spain	Cazorla	Caz*	37.81	-2.96	<i>Pinus</i>	<i>nigra</i>	1816	1900	2006	107	33.48
Turkey	Elmali	Elm**	36.60	30.02	<i>Juniperus</i>	<i>excelsa</i>	1937	1900	2006	107	31.33
Morocco	Col du Zad	Col*	32.97	-5.07	<i>Cedrus</i>	<i>atlantica</i>	2200	1600	2000	401	32.72

Chronologies indicated by * were established within the EU-project ISONET, those indicated by ** were established within the EU project Millennium and those without asterisk were established within the Swiss Sinergia project iTREE. 'Ang' was developed by Labuhn et al.⁵⁷, 'Cze' by Büntgen et al.¹⁵ and 'Ger' by Konter et al.⁵³. Lowest and highest mean $\delta^{18}\text{O}$ value for the period 1900 to 1994 is indicated with bold and bold italic letters respectively.

Extended Data Table 2 | Normalized mean VPD values of the period 1991 to 2020 and 2011-2020 respectively, as derived from observations and multi-model means together with the values simulated by individual models

Regions	1991-2020				2011-2020			
	SF	WE	ECE	AP	SF	WE	ECE	AP
Observations	0.67	1.52	1.55	2.09	0.77	2.10	2.36	2.96
Multi-model mean	0.48	0.62	0.46	1.17	0.95	1.23	1.06	1.82
ACCESS-ESM1-5	0.64	0.55	0.61	1.09	1.30	1.13	1.36	1.67
CESM2	0.56	0.39	0.69	1.09	1.30	1.18	1.79	1.95
CMCC-ESM2	1.84	1.80	1.48	2.41	1.97	2.81	2.17	3.30
CNRM-ESM2-1	0.28	0.82	-0.03	1.09	0.72	1.51	0.61	1.77
CanESM5	1.18	1.51	1.09	1.77	1.65	2.17	1.57	2.62
EC-Earth3-Veg	-0.12	-0.19	0.12	0.58	-0.05	0.05	0.82	1.21
GFDL-ESM4	-0.29	-0.04	-0.09	0.34	0.24	0.50	0.43	0.43
IPSL-CM6A-LR	1.17	1.41	0.73	2.31	2.00	2.35	1.54	3.34
MIROC-ES2L	-0.62	-0.44	-0.42	0.42	-0.37	0.05	0.15	1.10
MPI-ESM1-2-LR	0.18	0.05	0.44	0.75	0.24	0.03	0.26	0.80
MRI-ESM2-0	-0.01	0.36	0.10	0.54	0.23	0.90	0.23	1.11
UKESM1-0-LL	0.96	1.22	0.80	1.63	2.15	2.03	1.83	2.57